DOI:10.1002/smll.201701555
Full Paper

Laser-Induced Focused Ultrasound for Cavitation Treatment: Toward High-Precision Invisible Sonic Scalpel

*Taehwa Lee, Wei Luo, Qiaochu Li, Hakan Demirci, and L Jay Guo**

Dr. T. Lee, Prof. L. J. Guo
Department of Mechanical Engineering
The University of Michigan
Ann Arbor, MI 48109, USA
E-mail: guo@umich.edu

Dr. W. Luo, Q. Li, Prof. L. J. Guo
Electrical Engineering and Computer Science
The University of Michigan
Ann Arbor, MI 48109, USA

Prof. W. Luo
School of Optical and Electrical Information
Huazhong University of Science and Technology, China

Prof. H. Demirci
Kellogg Eye Center
The University of Michigan
Ann Arbor, MI 48109, USA

Keywords: micro-cavitation, laser ultrasound, tissue cutting

Beyond widely exploited functional imaging based on photoacoustic effect, we demonstrate a new application of the photoacoustic effect for high-precision sonic cutting of water-based soft materials using micro-cavitation induced by focused photoacoustic pulses. Pulsed optical excitation of an efficient photoacoustic layer coated on a concave surface generates focused photoacoustic pulses, which are strong enough to produce cavitation microbubbles within the focal region (lateral focus < 100 μm). This leads to controlled micro-cavitation, which can be used to cut or ablate soft tissue in a precise manner. We demonstrate precise cutting of tissue-mimicking gels as well as diseased eye tissues.

1. Introduction

The photoacoustic (PA) effect (light-to-sound conversion) has been widely used for various applications due to its non-contact, non-destructive characteristics. In these applications, pulsed (or modulated) light is irradiated on light absorbing materials, producing PA signals via transient heating followed by thermal expansion of the materials, and measurement of the PA signals allows to determine certain properties of the materials. With pulse laser, PA systems can generate broadband ultrasound pulses, which are useful in high-resolution imaging and sensing, e.g., PA imaging for structural, functional, and molecular imaging.[1-4] Beyond PA imaging, new applications of the PA effect have been recently investigated, which include all optical fiber-based ultrasound imaging[5, 6] and therapeutic applications using high-amplitude photoacoustic pulses.[7-9] Notably, these applications used PA transmitters consisting of PA converting films coated on transparent substrates.[10-13] Similar to piezoelectric transducers, PA transmitters deliver the ultrasound pulses to the issue in a non-contact manner. Baac *et al.* demonstrated focused PA pulses generation using a PA transmitter composed of a concave optical lens with a PA coating layer made of a carbon nanotube (CNT) composite (will be referred as CNT lens). The focused PA pulses by the CNT lens were strong enough to cause micro-cavitation bubbles on a acoustically hard boundary in water.[14] Also, violent growth and collapse of the microbubbles was demonstrated to cause targeted mechanical disturbance on the cells cultured on glass substrates,[7, 15, 16] showing great promise for high-precision targeted cavitation therapy.

We should note that micro-cavitation alternatively generated by pulse laser via optical breakdown or vaporization, has been studied for a long time and even used for therapeutic applications such as laser surgery of soft water-rich tissue.[17, 18] However, such optical approach towards micro-cavitation is limited to transparent tissue or superficial tissue due to the limited optical penetration. Histotripsy, which relies on acoustic cavitation induced by tightly focused ultrasound pulses, has shown great promise in targeted cavitation therapy by fractionating tissue into acellular homogenate, while minimizing unwanted thermal damages to tissue.[19, 20] The non-thermal, mechanical effects produced

by histotripsy are different from that in typical high intensity focused ultrasound (HIFU), often producing uncontrolled cavitation over a relatively large focal volume (> mm) accompanied by unwanted thermal damage.[21] To achieve negative pressure amplitudes ($P_- > 20$ MPa) higher than cavitation threshold, histotripsy requires relatively large aperture of piezoelectric transducers for high focal gain, which, however, may have the limited acoustic window when treating deep-tissue and thus need to further increase pressure amplitudes.[22] Although relatively large focal volume produced by histotripsy is effective in treating large lesions, it would be challenging to achieve micro-precision cavitation treatment.

The photoacoustic micro-cavitation by laser generated focused ultrasound (LGFU) with its tight focal volume (~100 μm) could be useful for unprecedented high-precision cavitation therapy applicable to vital organs such as brain and eyes where small lesions are surrounded by vulnerable nerves. Additionally, compact PA transmitters (< 15 cm) allows a easier experimental setup, and can be further integrated to endoscope. However, the main limitation of photoacoustic micro-cavitation previously demonstrated was that targets such as cells or tissue should be placed on an acoustically hard substrate (e.g., glass) to take advantage of the pressure doubling near the substrate for cavitation inception.[14] Without the rigid substrate, photoacoustic pulses in a free field were not strong enough to cause micro-cavitation, thus making it difficult to treat tissue far away from the rigid substrate.

In this work, we demonstrate high-precision cavitation cutting and treatment of water-rich soft materials, which is enabled with micro-cavitation (<100 μm) in a free field, produced by laser-generated focused ultrasound.[23] The cavitation-based sonic cutting is capable of precisely cutting tissue-mimicking gels into primitive shapes as well as complex shapes with small kerf of <50 μm. In addition to the cutting mode, this approach can accurately ablate certain volume of tissue-mimicking gel, and is also applied to intestinal cell spheroids (called organoids) and pig eyeball. This modality could open new possibilities in non-invasive surgery of small lesions, which can minimize side effects associated with any unnecessary cutting and bleeding while protecting normal nerves and tissue near malignant tissue.

2. Results and Discussion

2.1. High-Precision Cutting of Tissue-Mimicking Gel

Figure 1a shows the schematics of a cavitation treatment setup consisting of laser-generated focused ultrasound system and a 3-axis motorized stage. Pulsed laser beam (pulse duration: 6 ns, wavelength: 532nm) is irradiated onto a thin carbon nanotube (CNT) composite film coated on the concave side of a plano-concave optical lens, producing photoacoustic pulses that converge at the center of curvature of the concave surface (Diameter D = 15 mm, radius of curvature $r = f$ = 9.2, and f-number = r/D = 0.61). The focused photoacoustic pulses (center frequency f_c = 15 MHz) are strong enough to create micro-cavitation in water (negative pressure amplitude P_- > 30 MPa).[23] The micro-cavitation is very controllable, as it can be regulated spatially within the focal volume and temporally within the pulse duration. Such controlled micro-cavitation is capable of localizing mechanical effects (disruption), allowing micro-cutting of water-based materials such as agarose gel. In the experiment, both laser beam and the PA lens are fixed and thus cavitation remains at a certain location, while the samples are precisely moved through a motorized stage with micrometer resolution.

Figure 1b illustrates the schematics of cavitation-based ultrasonic cutting of a penetrating square hole ($x \times y$ = 1 mm^2). The thin tissue-mimicking gel of 1 mm thickness is sequentially cut by moving the cavitation traces along four imaginary surfaces enclosing the square, whose z-direction penetrates through the 1 mm gel. By controlling the moving stage step of Δx (or Δy) = 50 μm and Δz = 50 μm, cavitation cutting is conducted at a laser pulse energy of 16 mJ/pulse (corresponding negative pressure amplitude, P_- = 30 MPa). The applied negative pressure amplitude is higher than the bubble nucleation threshold ~ 24 MPa

(nucleation threshold is defined when the probability of the observed cavitation is equal to 1). The cut-out cube (1×1 mm^2) and the hole left behind the gel are shown in Figure 1b. Also, the other primitive shapes (circle and triangle) are easily produced with the cavitation cutting (**Figure 1c**), all exhibiting sharp cut edges.

To demonstrate the capability of the high-precision cavitation cutting applicable to more complex shapes beyond primitive shapes, we perform the cavitation cutting of shapes in the form of the University of Michigan (M) logo and the US mainland, as shown in **Figure 2c and 2f**. The cavitation cutting is conducted along the predefined paths that are extracted from the outline of the images and are scaled to a width of 3 mm, as shown in **Figure 2a and 2d**.

Photographs of the as-cut gel samples are shown in **Figure 2b and 2e**. In Figure 2b, the straight lines carved on the thin gel are clearly seen, having a kerf of approximately 45 μm. Although the cut inner part is structurally detached from the outside, water surface tension kept them together, requiring a gentle push of the inside part for separation. As compared to the M shape, the outline of the US map consists of more complex curves. Both the inner and outer parts are well separated after the cutting, as shown in Figure 2f. Note that the narrow and long region of Florida (only 100 μm in width) is successfully preserved.

To show an advantage of our sonic cutting approach over the traditional laser cutting, the cavitation-based cutting is applied to black gels having significantly limited optical penetration. The M logo is carved on the black gel, shown in **Figure 3**. The kerfs on the top and bottom surface of the black gel remain the same, indicating the uniform cutting depth. Although laser cutting based on dielectric breakdown shows promise in cutting of transparent materials, it is limited in cutting opaque materials, especially when they are buried by another opaque material. This indicates that our cavitation-based cutting approach could be

potentially applied to tissues deep inside the body, as long as the laser-generated ultrasound pulses are not significantly attenuated during propagation.

2.2. Characterization of Micro-Cavitation

Figure 4 shows shadowgraph images of photoacoustic (PA) pulses and micro-cavitation in water (a) and tissue-mimicking gel (b) at a laser pulse energy of E = 18.5 mJ/pulse (corresponding to P_- = 35 MPa), which is slightly higher than that used in the cutting experiment in order to create larger bubbles for easier observation. In both cases, the visualized PA waves generated from the PA lens, converge at the focus (t = 0.1 μs). After the PA pulses pass through the focus, bubble clouds are clearly observed within the focal region (t = 0.2 μs). The bubbles rapidly grow, coalesce and then collapse; the bubble lifetimes (t_l) are about 25 μs in water and 11 μs in the gel before final collapse. The shorter lifetime in the gel is because the gel confines the bubble growth, and thus the maximum bubble in the gel is smaller than that in water. Note that the bubble lifetimes are much greater than the negative duration of the PA pulses (< 100 ns),. Therefore, the PA pulses strongly influence bubble nucleation and initial growth, while the rest of bubble dynamics in the absence of pressure field is driven by inertia.

Under the strong pressure pulse, tiny bubbles are densely nucleated within the focal volume, which has an elliptical shape elongated along the z-axis ($l_r < l_z$, where l_r, l_z are the *r*-width and *z*-width), as dictated by the focused pressure field as shown in the simulation (**Figure 5a)**. The dark red region ($\sigma_{sim} = l_r / l_z$ = 0.3) corresponds to the region with high pressure amplitude. As shown in **Figure 5b**, the visualized bubble region in water ($\sigma_{vis} = l_r / l_z$ = 95 μm /285 μm = 0.33 at t = 0.4 μs) shows a good match with the simulated

focal region (σ_{sim} = 0.3) since bubble nucleation region is determined as an area where negative pressure amplitudes are greater than cavitation threshold. The simulation was carried out using the acoustic module in COMSOL Multiphysics. The kerf measured in the cutting demonstration (45 μm) is much smaller than the largest bubbles in the gel (e.g. t = 6 μs), while it is similar to the lateral width of the bubble nucleation region (t = 0.2 μs). This finding suggests that explosive bubble growth at the early stage after its inception is more destructive than the later bubble growth, and thus is responsible for the cutting.

Figure 6 shows that cutting performance by varying laser pulse energy and thus pressure amplitude. For the lowest pressure amplitudes (but above the cavitation threshold), the inner part cannot be removed from the gel after cutting, because the bubble nucleation region is not large enough to produce a connected cutting track for cut step of $\Delta x = \Delta y$ = 50 μm. With increasing pressure amplitude, the bubble nucleation region increases, and eventually form a well-connected path that completes the cutting.

The number of the tiny bubbles (n_B) is estimated to be n_B > 30 based on shadowgraphy images, corresponding to an average bubble space of $d < 20\,\mu\text{m}$. Such short inter bubble distance can cause strong bubble-bubble interaction as the non-dimensional standoff distance $\gamma = d/(2R_{\max}) < 1$,[24] where $R_{\max}$ is the maximum bubble radius that is calculated for an isolated single bubble ($R_{\max} = 30$ μm for P_- = 35 MPa) by using the Rayleigh-Plesset equation.[25] In the strong interaction regime, expansion of the individual bubbles is significantly restricted, leading to the maximum radius of the merged bubbles ($R^*_{\max} = 200$ μm in water), which is much smaller than the estimation based on $n_B R_{\max}$, i.e., $R^*_{\max} < n_B R_{\max} = 900$ μm.

Most of the tiny growing bubbles coalesce into larger bubbles. However, it is interesting to note that in water, some of the bubbles nucleated in the periphery of the cloud are observed to leave from the focal region (see arrows in the images), preferentially moving up due to the buoyancy. This is because violent bubble growth can lead to bouncing bubbles without causing rupture of the liquid film between the bubbles instead of merging bubbles. It is well known that two bubbles bounce rather than coalesce if their relative approach velocity is sufficiently high (i.e., high Weber number, $W_e = \rho V^2 R_{\max} / \sigma > 10$).[26] The individual bubbles that are closely packed will rapidly expand due to the strong pressure pulse, thus falling into the bouncing regime (estimated bubble growth speed of $V \sim 150$ m/s, $W_e > 10^3$). However, only the outer bubbles can escape from the cloud, whereas the inner bubbles surrounded by the outer bubbles remain in contact with the surrounding bubbles, resulting in their coalescence. On the other hand, no bubble departure is observed in gel; the bubbles stay within the focal region, merging into larger bubbles due to gel confinement.

2.3. Volumetric Ablation of Tissue-Mimicking Gel

Our cavitation-based sonic cutting approach shows promise in high-precision micro-cutting and potential to micro-surgery of diseased tissue. Not only can diseased tissue be cut out from healthy surroundings, but also they can be mechanically ablated for treatment of the entire volume of the tissue. Cells constituting tissue can be fractionated to acellular homogenates by localized mechanical effects associated with micro-cavitation, which is similar to histotripsy.[20] The cavitation-based ablation approach is illustrated in **Figure 7a**. A chunk of transparent gel (5×5×10 mm^3) was partially ablated through a scanning volume of 0.5×0.5×3 mm^3 (colored purple) at a laser pulse energy of E = 17.5 mJ/pulse; micro-cavitation was applied on x-y planes (Δx, Δy = 50 μm), while moving along the z axis with a

spacing of 50 μm. For easy alignment, the z length of the cavitation scanning volume (3 mm) is much greater than the actual depth of the ablation volume. As shown in **Figure 7b**, the cavitation-based ablation was conducted for square trenches on the surface of the gel block under conditions of two different intervals (Δx, Δy, Δz = 50 or 100 μm). For the large interval (100 μm), the ablation effect was not significant, only showing numerous dark spots separated apart on the gel surface. This result indicates that the spacing is too large to form a continuous treatment volume. However, for the small interval (50 μm), the deep trench was successfully produced on the gel block, whose depth corresponds to the overlap between the cavitation scanning volume and the gel block.

2.4. Application to Tissues

2.4.1. Intestinal cell spheroids (called organoids)

To demonstrate the capability of the cavitation-based treatment of tissue, we used intestinal cell spheroids (called organoids), which are a three-dimensional organ-bud grown in vitro that shows realistic micro-anatomy. The human intestinal organoids are believed to be the stimulated micro human organs which has more similarity than the other 3D structures.[27, 28] Cell spheroids with a volume of approximately 1 mm^3 are fixed in metrigel and immersed in 20% Fetal Bovine Serum (FBS) cell culture media, and then located right at the focus of the PA lens. The spheroids were scanned by a 3D stage for a whole treatment volume of $0.8\times0.8\times1.7$ mm^3 (Δx, Δy, Δz = 50 μm); at a laser pulse energy of E = 17.5 mJ/pulse). The treated sample and a control sample were then imaged by a fluorescent microscope (Olympus BX-51). As seen in **Figure 8**, the ablated spheroid (dashed square mark) were clearly observed.

2.4.2. Pig eyeball

The pig eye is similar in size and structure to human eye and contains vitreous humor, a water-based gel. It also has a thick outer layer that is called sclera. This thick outer layer can affect the acoustic propagation and thus therapeutic outcomes. Using a pig eye to create cavitation ablation can provide information that could be applicable to human eyes. To demonstrate this effect, we cut the pig eye into a piece of 5×5 mm^2 for easy visual confirmation of therapeutic effects and for easy mounting to the cavitation ablation system, as shown in **Figure 9a**. The piece contains a thick Scleral outer layer, vascular choroidal layer and retinal nerve layer. To investigate the effect of the thick scleral outer layer on PA propagation, two different settings are used, as shown in **Figure 9b and 9c**. First, PA pulses are directly focused on the vascular dark-colored choroid without passing through the thick sclera (**Figure 9b**). In the other setting, the piece is flipped so that PA pulses pass through the sclera and are focused on the choroid (**Figure 9c**). The cavitation ablation is conducted for two square trenches spaced with 0.2 mm, each trench of 0.5×0.5 mm^2. For both settings, mechanical ablation is visually confirmed, showing two small ablated trenches on the choroid after drying the samples. However, the sclera layer caused the acoustic attenuation when PA pulses pass through it, thus requiring compensation by applying slightly higher laser pulse energy (E = 20 mJ/pulse).

3. Conclusions

We have demonstrated the cavitation-based sonic scalpel by using laser-generated focused ultrasound. Owing to micro-cavitation regulated by the laser-generated focused ultrasound, such sonic scalpel can accurately cut or ablate water-rich materials such as tissue-mimicking gel and tissues in a targeted, high-precision manner. The resolution of our sonic

cutting was ~ 50 μm, as confirmed with the kerf after the cutting experiment. Since the sonic scalpel is based on non-thermal cavitation produced by short PA pulses (~ 50 ns), thermal effects are negligible. Temperature increase by the short pulses is conservatively estimated to be 10^{-2}°C (see supporting information). Our cavitation-based sonic scalpel could be applicable to targeted, non-invasive surgery, where one can treat diseased tissues while minimizing the collateral damage to the healthy surrounding tissues.

Recent advancement in imaging modalities has allowed to accurately evaluate disease margins with improved imaging resolution. Combined with these imaging modalities, our high-precision sonic scalpel will be effective in treating early-diagnosed small lesions or lesions close to nerves. Specifically, our approach can be implemented for prevision, targeted surgery of brain, because inaccurate treatment can cause brain damage. By isolating diseased lesions (e.g. tumor) in the brain from the surrounding through the cavitation treatment, the diseased tissues are likely to be killed over time. This is because except for some rare cases, brain cells barely regenerate or regenerate slows and thus the isolated regions cannot get sufficient blood supply and nutrients.

Our cavitation-based sonic treatment can be readily customized by optimizing ultrasound parameters depending on surgical applications. By tuning laser pulse duration and photoacoustic coating layers, ultrasound frequency can be adjusted in a way that potential acoustic attenuation is minimized when targets are located deep in the body. Because the center frequency of the PA pulses is ~15 MHz, pressure amplitudes decrease by 60% for 5 mm propagation in tissues (e.g., attenuation coefficient of 1 $dBcm^{-1}MHz^{-1}$ for kidney). Also, PA lens geometry can be chosen to have a proper focal length and *f*-number for improved cavitation performance. Moreover, time duration of the cavitation treatment can be reduced by using pulse laser with higher pulse repetition rate.

4. Experimental Section

Laser-generated focused ultrasound: Photoacoustic pulses are generated by irradiating pulsed laser beam (Nd:YAG laser, FWHM = 6 ns, wavelength = 532 nm) onto a carbon nanotube (CNT)-PDMS composite coated on the concave side of a plano-concave fused silica lens (purchased from Optosigma, Santa Ana, CA) with 9.2 mm radius of curvature and 15 mm diameter. The PA pulse generated by a laser pulse is geometrically focused on the center of the concave. The focused PA pulses generated by the PA lens have a pulse duration of ~50 ns, negative pressure amplitudes of >30 MPa and the center frequency of ~15 MHz (see Figure S1 in the supporting information). Further details on characterization of the focused PA pulses can be found in our previous paper [23]. To fabricate the CNT-PDMS composite-coated lens[7, 10], catalyst layers of Fe (~1 nm) and Al2O3 (~3 nm) were first coated on the concave surface of the plano-concave lens. Then, multi-walled CNTs were grown on the concave surface in a mixture of C_2H_4/H_2/He in an atmospheric pressure tube furnace at 770°C. PDMS elastomer was then spin-coated on the CNT-grown surface at 3000 r.p.m. for 1 minutes, and then cured at 100°C for 1 hour. The CNT-PDMS composite consists of CNTs embedded in PDMS. The CNT composite serves as an excellent light-to-sound converter, because the CNTs efficiently absorb an incident optical energy (> 80%) and convert it to heat that is rapidly transferred to the surrounding PDMS with a high thermal expansion coefficient.

Laser flash shadowgraphy: Laser-induced acoustic waves and bubbles are visualized by laser-flash shadowgraphy. This imaging technique is a pump-probe method that allows a probe laser pulse (Diode-pumped solid-state laser, FWHM = 5 ns, 527 nm, Laser-export

Co.Ltd) to obtain shadow images of the bubbles at a different temporal moment specified by the time delay between the pump (Nd:YAG laser) and the probe pulses through a delay generator (Stanford Research Systems, DG535). The shadowgraphs are captured with a CCD camera with very slow shutter speed (~ ms), but with an exposure time of 5 ns determined with probe laser, allowing imaging of fast-moving objects.

Preparation of tissue-mimicking gel: Agarose phantoms were used to provide a well-controlled elastic medium for this study. Agarose phantoms of 1% w/v were prepared by slowly mixing agarose powder (Agarose Type VII, Sigma-Aldrich) into pure water heated at 95 °C. The solution was stirred on a hot plate until the gel turned completely transparent. Agarose solutions were degassed under a partial vacuum of 1 kPa for 30 min and then was poured into 7.5 × 2.5 × 0.1 cm rectangular glass tissue phantom holders. The tissue phantom holders were placed in a refrigerator at 4°C to allow the agarose solution to solidify before use.

Preparation of intestinal organoids and imaging method: Firstly, pluripotent stem cells are treated with activin A for 3 d and are differentiated into $FOXA2^{+}SOSOX17^{+}$ endoderm. Then, a patterning step is performed to the pluripotent stem cells using FGF4 and WNTNT3a. They were patterned into CDX2 + mid- and hindgut tissue and 3D mid- or hindgut spheroids bud from the monolayer epithelium attached to the tissue culture dish could be found after this step. After that, these 3D spheroids with prointestinal growth factors are further cultured in Matrigel. The 3D spheroids proliferate and expand over several days to give rise to intestinal organoids with suitable sizes.[29] The organoid sample was stained by EthD-1 and Calcein AM [Thermo fisher live/dead cell viability kit] with the volume of 20ul and 5ul

respectively in 10ml hanks solution in petri dish for 30mins. Then the sample was imaged with fluorescent microscope[BX-51] under illumination light of 510-550nm wavelength for dead cell tracking. However, we just used this method to keep track of the morphology or contour of the organoids instead of differentiating live and dead cells carefully, because the cells in the treated region is depleted rather than simply killed.

Preparation of pig eyeball: Pig eyes were harvested by adhering to all standards set forth in the ARVO Statement for the Use of Animals in Ophthalmic and Visual Research. After the eye was enucleated, a 5×5 mm piece of pig eye was cut from the posterior pole of the globe and treated.

Pressure Field Simulation: To calculate pressure field around the focus, the linear wave equation in a lossless medium is solved by using a finite element method (Courant number < 0.05; COMSOL Multiphysics 4.3b). For simplicity, the nonlinear wave propagation and attenuation are assumed to be negligible, because we focus on the acoustic propagation in a small region near the focus (< 1 mm). Instead, a proper incident pressure on the optoacoustic lens is chosen to match the measured signal at the focus. The simulated pressure field around the focus is obtained with the maximum negative pressure amplitude encountered at each location during the simulation.

Acknowledgements
This work was supported by MCube program at the University of Michigan. T. Lee and W. Luo contributed equally to this work. We acknowledge Dr. Shuichi Takayama and Nick Ginga for providing the intestinal organoids for the testing.

Received: ((will be filled in by the editorial staff))
Revised: ((will be filled in by the editorial staff))
Published online: ((will be filled in by the editorial staff))

References

[1] M. Xu and L. V. Wang, *Rev. Sci. Instrum.* **2006***, 77*, *041101*.

[2] A. de la Zerda, J.-W. Kim, E. I. Galanzha, S. S. Gambhir, V. P. Zharov, *Contrast Media Mol. Imaging* **2011***, 6*, 346.

[3] K. Pu, A. J. Shuhendler, J. V. Jokerst, J. Mei, S. S. Gambhir, Z. Bao, J. Rao, *Nat. Nanotech.* **2014**, *9*, 233.

[4] C. Kim, C. Favazza, L. V. Wang, *Chem. Rev.* **2010**, *110*, 2756.

[5] R. J. Colchester, E. Z. Zhang, C. A. Mosse, P. C. Beard, I. Papakonstantinou, A. E. Desjardins, *Biomed. Opt. Express* **2015**, *6*, 1502.

[6] R. J. Colchester, C. A. Mosse, D. S. Bhachu, J. C. Bear, C. J. Carmalt, I. P. Parkin, B. E. Treeby, I. Papakonstantinou, A. E. Desjardins, Appl. Phys. Lett. **2014**, *104*, 173502.

[7] H. W. Baac, J. G. Ok, A. Maxwell, K.-T. Lee, Y.-C. Chen, A. J. Hart, Z. Xu, E. Yoon, L. J. Guo, *Sci. Rep.* **2012***, 2*, 989.

[8] J. Di, J. Kim, Q. Y. Hu, X. N. Jiang, and Z. Gu, *J. Control.Release* **2015***, 220*, 592.

[9] T. Lee, H. W. Baac, J. G. Ok, H. S. Youn, and L. J. Guo, *Phys. Rev. Appl.* **2015***, 3*, 044007.

[10] H. W. Baac, J. G. Ok, H. J. Park, T. Ling, S.-L. Chen, A. J. Hart, L. J. Guo, *Appl. Phys. Lett.* **2010***, 97*, 234104.

[11] W. Y. Chang, W. B. Huang, J. Kim, S. B. Li, and X. N. Jiang, *Appl. Phys. Lett.* **2015***, 107*, 161903.

[12] R. J. Colchester, C. A. Mosse, D. S. Bhachu, J. C. Bear, C. J. Carmalt, I. P. Parkin, B. E. Treeby, I. Papakonstantinou, A. E. Desjardins, *Appl. Phys. Lett.* **2014***, 104*, 173502.

[13] B.-Y. Hsieh, J. Kim, J. Zhu, S. Li, X. Zhang, and X. Jiang, *Appl. Phys. Lett.* **2015***, 106*, 021902.

[14] T. Lee, H. W. Baac, J. G. Ok, H. S. Youn, and L. J. Guo, *Phys. Rev. Appl.* **2014***, 2*, 024007.

[15] H. W. Baac, J. Frampton, J. G. Ok, S. Takayama, and L. J. Guo, *J. Biophotonics* **2013***,* 6.

[16] H. W. Baac, T. Lee, and L. J. Guo, *Biomed. Opt. Express* **2013***, 4*, 1442.

[17] I. Toytman, A. Silbergleit, D. Simanovski, and D. Palanker, *Phys. Rev. E* **2010***, 82*, 046313.

[18] A. K. Jayasinghe, J. Rohner, and M. S. Hutson, *Biomed. Opt. Express* **2011***, 2*, 2590.

[19] W. W. Roberts, T. L. Hall, K. Ives, J. S. Wolf, J. B. Fowlkes, and C. A. Cain, *J. Urol.* **2006***, 175*, 734.

[20] Z. Xu, T. L. Hall, J. B. Fowlkes, and C. A. Cain, *J. Acoust. Soc. Am.* **2007***, 122*, 229.

[21] T. J. Dubinsky, C. Cuevas, M. K. Dighe, O. Kolokythas, and J. H. Hwang, *Am. J. Roentgenol.* **2008***, 190*, 191.

[22] E. Vlaisavljevich, O. Aydin, K.-W. Lin, Y. Yuksel Durmaz, B. Fowlkes, M. ElSayed, Z. Xu, *Phys. Med. Biol.* **2015***, 61*, 663.

[23] T. Lee, J. G. Ok, L. J. Guo, and H. W. Baac, *Appl. Phys. Lett.* **2016***, 108*, 104102.

[24] I. van der Kroon, P. A. Quinto-Su, F. F. Li, and C.-D. Ohl, *Phys. Rev. E* **2010***, 82*, 066311.

[25] C. E. Brennen, *Cavitation and Bubble Dynamics*, Oxford University Press, Oxford, United Kingdom **1995**.

[26] P. C. Duineveld, *Appl. Sci. Res.* **1998***, 58*, 409.

[27] J. R. Spence, C. N. Mayhew, S. A. Rankin, M. F. Kuhar, J. E. Vallance, K. Tolle, E. E. Hoskins, V. V. Kalinichenko, S. I. Wells, A. M. Zorn, N. F. Shroyer, J. M. Wells, *Nature* **2010***, 470*, 105.

[28] C. Xinaris, V. Brizi, G. Remuzzi, *Nephron.* **2015***, 130*, 191.

[29] K. W. McCracken, J. C. Howell, J. M. Wells, J. R. Spence, *Nat. Protoc.* **2011***, 6*, 1920.

Figures

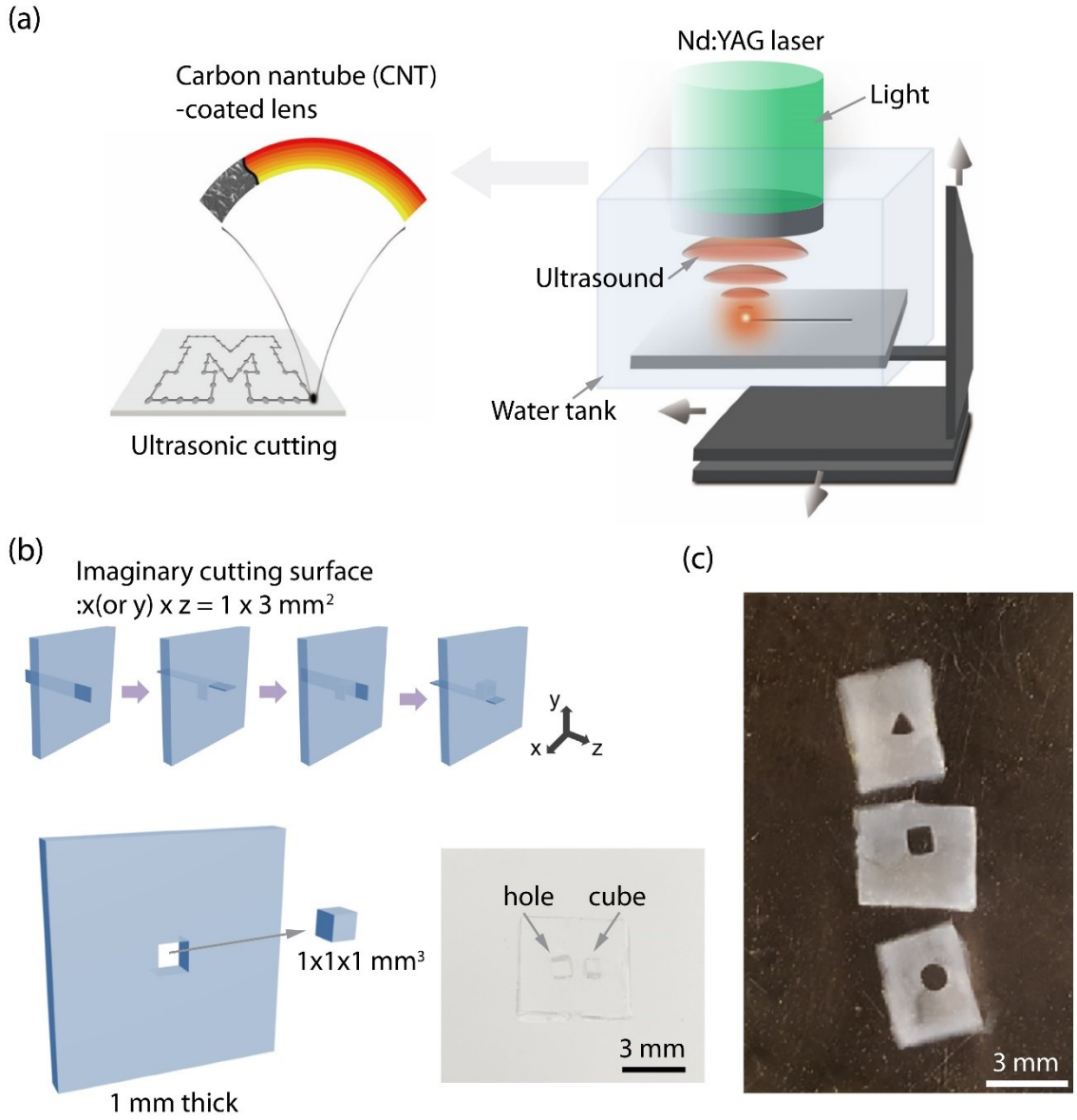

Figure 1. (a) Experimental setup for cavitation-based sonic cutting. (b) Schematics of sonic cutting of tissue-mimicking gel (1 mm thick) for hole and cube. Ultrasonic cutting on imaginary cutting surface was sequentially applied. Photo was taken after cutting experiment. (c) Other primitive shapes (circle and triangle).

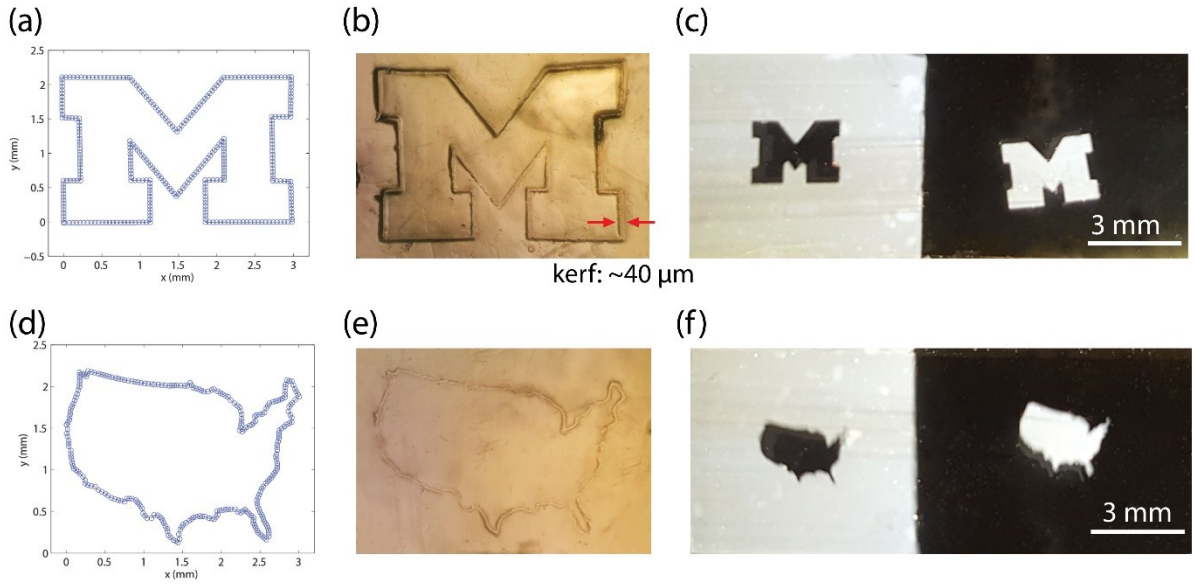

Figure 2. Cavitation-based sonic cutting of tissue-mimicking gel for complex shapes: the logo of University of Michigan, the United States map. (a) and (d) Predefined cutting paths. (b) and (e) Photos of the treated gels before removing the inner parts. The photos were taken by a microscope, looking yellowish. (c) and (f) Photos of the holes and the inner parts. The widths are 3 mm. The photos were taken by a digital camera.

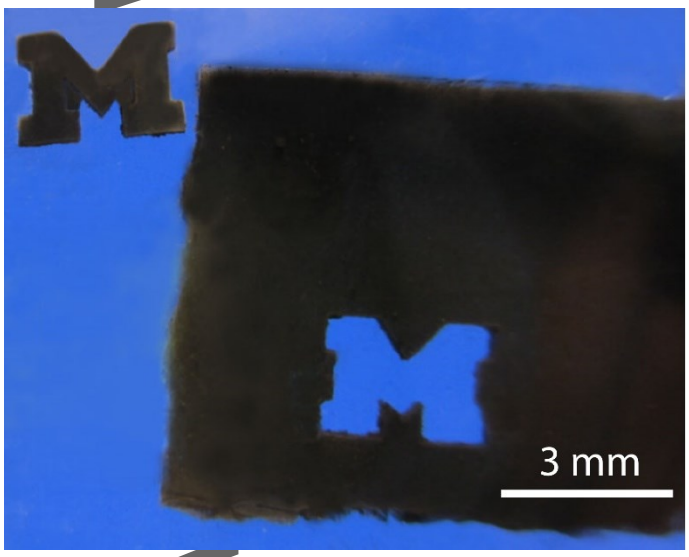

Figure 3. Cavitation-based sonic cutting of black tissue-mimicking gel.

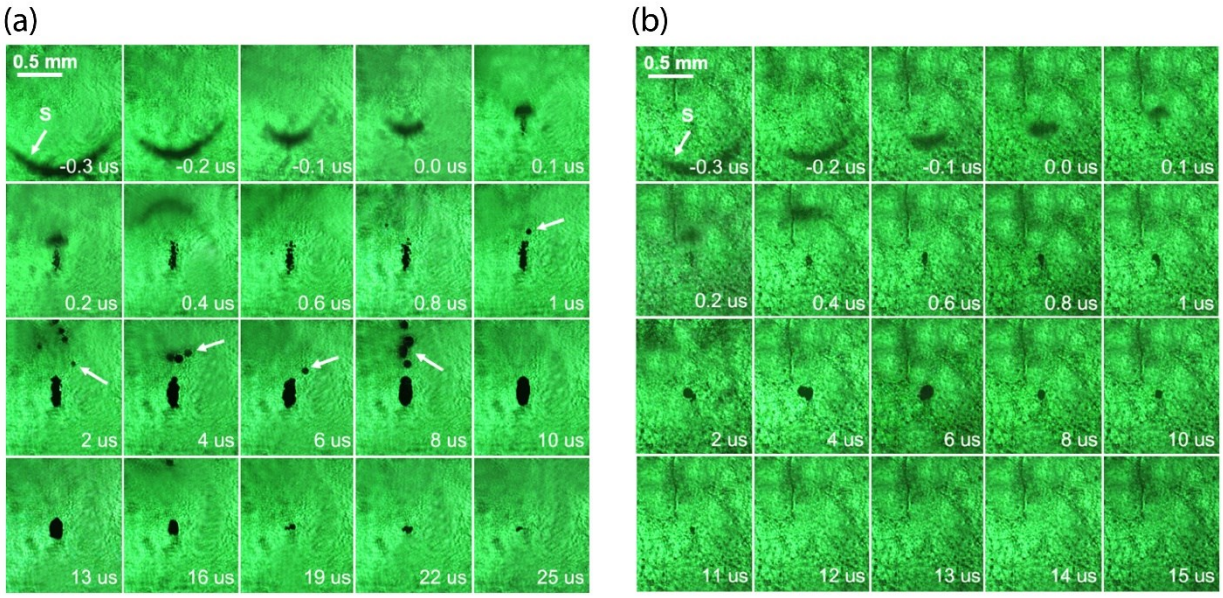

Figure 4. Shadowgraph images of micro-cavitation in water (a) and gel (b)

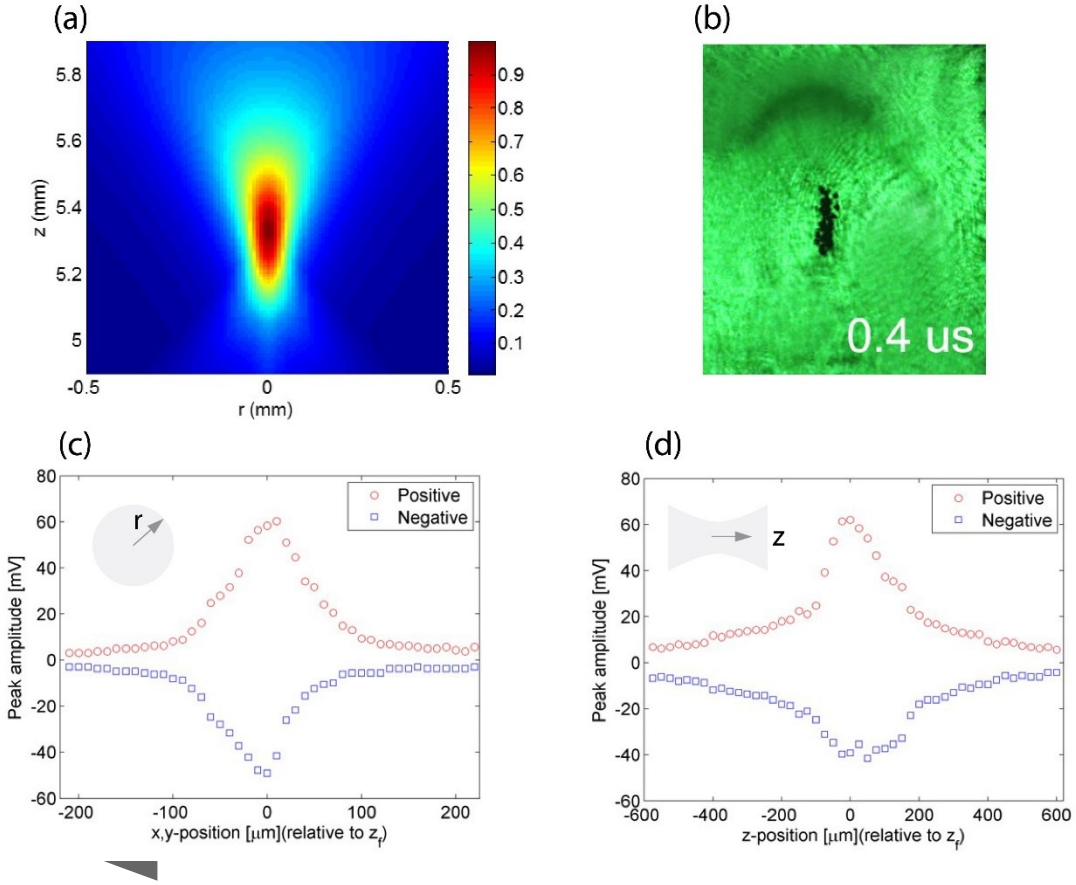

Figure 5. Characterization of focused photoacoustic pulses. (a) The simulated focal region. (b) Shadowgraph image of bubble nucleation region (t = 0.4 μs). Focal beam width in r-direction (c) and z-direction (d).

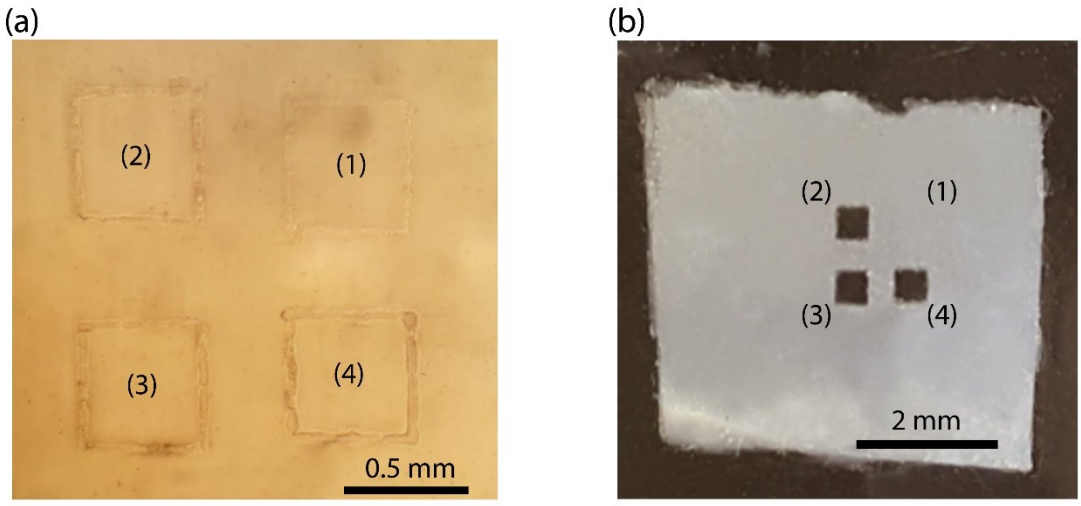

Figure 6. Cavitation-based sonic cutting at different laser pulse energies (E = 14, 16, 17.5, 18.5 mJ/pulse from (1) to (4)). (a) Photo of the treated gel having four squares before removing the inner parts. (b) Photo after removing the inner parts. For the lowest energy, the inner part cannot be removed.

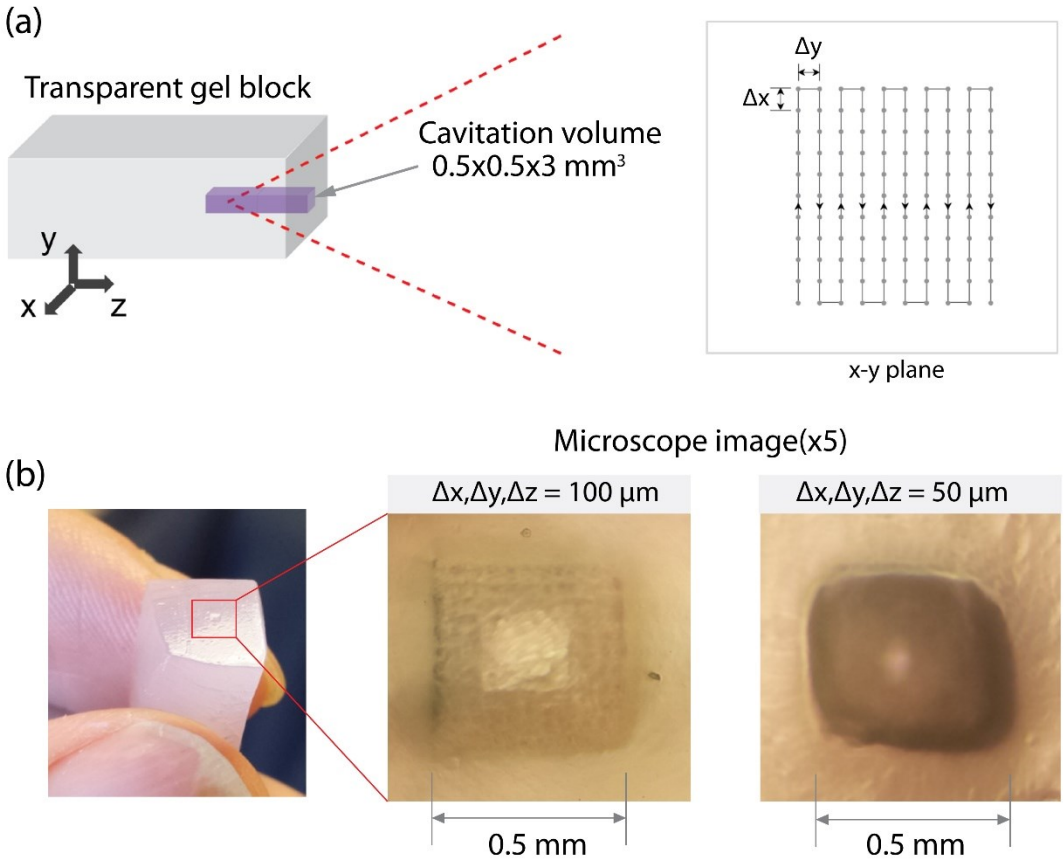

Figure 7. Cavitation-based volumetric ablation. (a) Illustration of the volume ablation (purple) of gel block. The cavitation volume of 0.5×0.5×3 mm^3 is formed by ablating x-y planes (Δx, Δy = 50 µm) at each z location (Δz = 50 µm). (b) Photos of the treated gel for two different intervals (Δ=50, 100 µm).

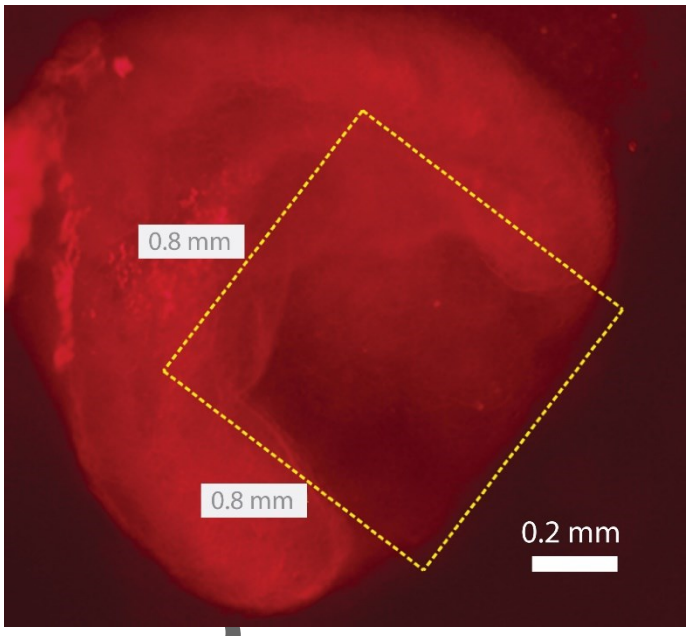

Figure 8. Cavitation-based volumetric ablation of Organoid

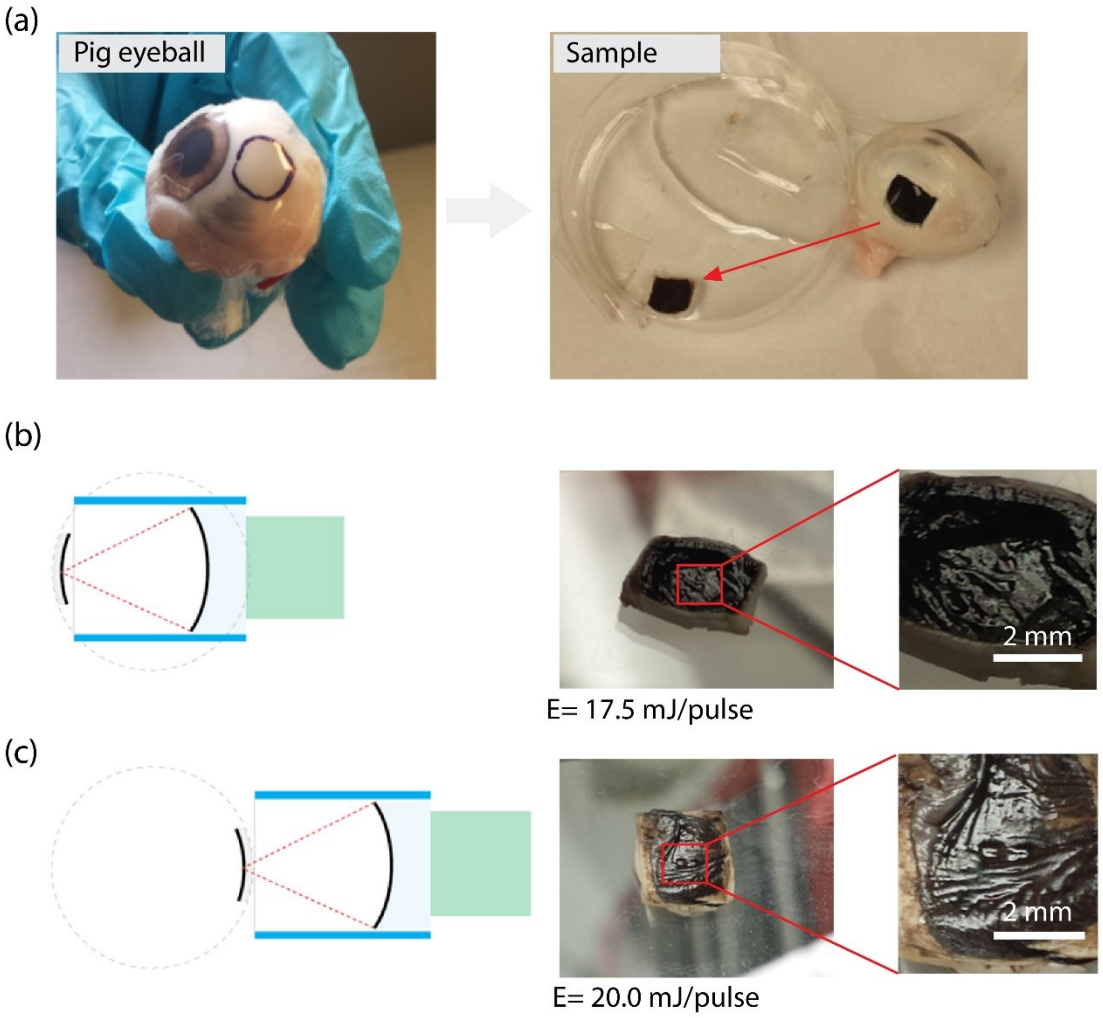

Figure 9. Cavitation-based volumetric ablation of pig eyeball. (a) Pig eyeball and the piece of the eyeball with a black Choroid layer and thick white Sclera layer. Photoacoustic pulses directly focused on the Choroid layer with (c) and without passing through the Sclera layer (b).

High precision sonic scalpel has been demonstrated using micro-cavitation generated by laser-generated focused ultrasound. Rapid growth of micro-bubbles causes strain of surrounding tissue, destroying tissue structures. Owing to controllable micro-cavitation, sonic ablation has high precision, which would be applicable for targeted treatment of diseased tissue.

Keyword

micro-cavitation;laser ultrasound;tissue cutting;carbon nanotube composite;photoacoustic effect

*Taehwa Lee, Wei Luo, Qiaochu Li, Hakan Demirci, and L Jay Guo**

Laser-Induced Focused Ultrasound for Cavitation Treatment: Toward High-Precision Invisible Sonic Scalpel

ToC figure